

Towards reconstructing the halo clustering and halo mass function of N-body simulations using neural ratio estimation

Androniki Dimitriou,^{1, 2, *} Christoph Weniger,^{2, †} Camila A. Correa,^{2, ‡}

¹*Instituto de Física Corpuscular (IFIC), Universitat de València-CSIC, E-46980, Valencia, Spain*

²*GRAPPA (Gravitation Astroparticle Physics Amsterdam), University of Amsterdam, Science Park 904, 1098 XH Amsterdam, The Netherlands*

Accepted XXX. Received YYY; in original form ZZZ

ABSTRACT

High-resolution cosmological N-body simulations are excellent tools for modelling the formation and clustering of dark matter haloes. These simulations suggest complex physical theories of halo formation governed by a set of effective physical parameters. Our goal is to extract these parameters and their uncertainties in a Bayesian context. We make a step towards automatising this process by directly comparing dark matter density projection maps extracted from cosmological simulations, with density projections generated from an analytical halo model. The model is based on a toy implementation of two body correlation functions. To accomplish this we use marginal neural ratio estimation, an algorithm for simulation-based inference that allows marginal posteriors to be estimated by approximating marginal likelihood-to-evidence ratios with a neural network. In this case, we train a neural network with mock images to identify the correct values of the physical parameters that produced a given image. Using the trained neural network on cosmological N-body simulation images we are able to reconstruct the halo mass function, to generate mock images similar to the N-body simulation images and to identify the lowest mass of the haloes of those images, provided that they have the same clustering with our training data. Our results indicate that this is a promising approach in the path towards developing cosmological simulations assisted by neural networks.

Key words: methods: numerical - methods: statistical - galaxies: haloes - cosmology: theory - dark matter

1 INTRODUCTION

High-precision galaxy surveys, such as Sloan Digital Sky Survey (SDSS; York et al. 2000; Abazajian et al. 2009), the Dark Energy Survey (DES; Dark Energy Survey Collaboration et al. 2016), the Dark Energy Spectroscopic Instrument (DESI; DESI Collaboration et al. 2016), EUCLID (Scaramella et al. 2021), and the upcoming Legacy Survey of Space and Time (LSST; LSST Science Collaboration et al. 2009; Ivezić et al. 2019), allow the detailed study of large scale structures and galaxy clustering statistics.

Interpreting the galaxy distribution in these surveys demands accurate theoretical predictions. A historical approach in the analysis of galaxy clustering lies in the analytic modelling of the formation and evolution of the dark matter haloes (Press & Schechter 1974; Bond et al. 1991; Mo & White 1996; Sheth & Tormen 1999). Even though this is one of the most active fields of astrophysics, it remains very challenging because of its multi-scale and multi-physics character. Cosmological numerical simulations (see e.g., Springel et al. 2005; Vogelsberger et al. 2020) are the method of choice for tackling the growing complexities at small scales. In these simulations dark matter builds the backbone for structure formation. Dark matter particles track the influence of gravity and are able to accurately reproduce clustering on small scales. Once we have access to these simulations, we identify real objects in them: dark matter haloes and

subhaloes (Springel et al. 2001; Behroozi et al. 2013) with which galaxies can be linked.

In the past few years, projects such as Eagle (Schaye et al. 2015), Horizon-AGN (Dubois et al. 2016), MassiveBlack-II (Khandai et al. 2015), the Illustris simulations (Vogelsberger et al. 2014a; Vogelsberger et al. 2014b; Pillepich et al. 2018), among others, have demonstrated that simulations of structure formation can reproduce many small-scale structural properties such as galaxy morphology and luminosity, galaxy stellar mass function and star formation rates of galaxies. These simulations are computationally expensive to produce, especially when baryonic physics and increasing resolution are included. To circumvent this problem, and exploit the wealth of data produced by cosmological simulations, machine learning has become a powerful tool (see e.g., Lucie-Smith et al. 2018; Aragon-Calvo 2019; Berger & Stein 2019; Alves de Oliveira et al. 2020; Arjona & Nesseris 2020; Ntampaka et al. 2020).

With the improvement in image recognition, classification and segmentation (e.g. Ronneberger et al. 2015), machine learning techniques have been applied in a large number of astronomical studies related to galaxy properties (e.g. Dieleman et al. 2015; Beck et al. 2018; Hocking et al. 2018; Dawson et al. 2020; Buck & Wolf 2021). In the context of halo modelling, machine learning algorithms have been implemented to predict galaxy properties based on halo formation and evolution (Xu et al. 2013; Agarwal et al. 2018; Wadekar et al. 2020; Lovell et al. 2021; Moews et al. 2021; Xu et al. 2021).

In this work, our goal is to measure the halo population parameters from a set of dark-matter-only cosmological simulations. Those

* E-mail: androniki.dimitriou@ific.uv.es

† E-mail: c.weniger@uva.nl

‡ E-mail: c.a.correa@uva.nl

simulations can be also thought of as parametric stochastic simulators, that take as input a set of physical parameters, sample many latent nuisance variables, and finally produce simulation data.

The applicability of likelihood based inference techniques, which are the golden standard to solve parameter inference problems in many areas, is severely limited in a high-dimensional setting, since they can be very time consuming, or inference is even impossible as the large number of parameters often leads to intractable likelihood functions. During the past years, likelihood-free inference techniques, also known as simulation-based inference, (Cranmer et al. 2020) have become state-of-the-art in solving various inverse problems by training neural networks (NN) to perform the mapping from observations to physical parameters. The main idea behind these techniques is to try to approximate posteriors instead of sampling from them. Likelihood-free inference is applied in several astrophysical contexts (see e.g., Birrer et al. 2017; Alsing et al. 2018; Alsing et al. 2019; Brehmer et al. 2019; Brehmer et al. 2019; Delaunoy et al. 2020; Coogan et al. 2020; Cole et al. 2021; Dax et al. 2021; Hermans et al. 2021b; Makinen et al. 2021; Villaescusa-Navarro et al. 2021a; Villaescusa-Navarro et al. 2021b; Zhao et al. 2022; Karchev et al. 2022; He et al. 2022 and Anau Montel et al. 2022).

Here, we construct an analytical forward toy model/simulator that generates images depicting the surface density of clustered dark matter haloes. We directly calibrate the model on dark-matter-only cosmological simulations using Marginal Neural Ratio Estimation (MNRE; Miller et al. 2020; Miller et al. 2021). This model contains four physical parameters: the number of haloes, N , the slope of the halo mass function, a , and two parameters of an effective clustering model, ϵ and n , as well as many latent nuisance variables which also control the spatial distribution of the haloes and are related to the halo mass function. We look for the best fit parameters on dark-matter-only simulations in order to reconstruct the halo mass function, to identify the lowest mass of the haloes in those simulations and to generate images which look similar to them.

The paper is structured as follows. In Section 2, we explain the structure of our forward model and we define its parameters. We also describe the process of its calibration on dark-matter-only simulation data generated by the EAGLE project (Schaye et al. 2015), using MNRE. In Section 3, we analyze the results that we obtain, focusing on reconstructing the halo mass function, as well as an artificial lower cutoff that we add at it. Finally, in Section 4, we summarize our results, we spot the limitations of our model and we discuss directions of future improvement.

2 METHOD

Our goal is to reconstruct the halo clustering and the halo mass function of dark-matter-only cosmological simulations, by directly calibrating an analytical toy halo model on them. The simulations that we use are described in Section 2.1, while a full description of our model and of the methodology that we follow for the calibration is presented in Section 2.2 and Section 2.3 respectively.

2.1 N-body simulation data

In this work, we use the dark matter-only cosmological simulations generated by the EAGLE project (Schaye et al. 2015). More specifically, we focus on the L025N0376 simulation, which corresponds to a comoving volume of 25 Mpc on a side with 376^3 dark matter

particles, each one having a mass of $1.15 \cdot 10^7 M_\odot$. Our toy halo model generates images that depict the surface density of clustered dark matter haloes. Since we want to compare these images with dark matter-only cosmological simulations images, we generate projected density maps of the 25 Mpc cosmological box. We do that by using the coordinates of the dark matter particles provided by the redshift zero simulation snapshot. Examples of these maps in units of $\frac{M_\odot}{\text{kpc}^2}$ and can be seen in Fig. 1.

Although the filaments observed in these images play a crucial role in galaxy evolution, very little is known about their number density and distribution and therefore it is very difficult to reproduce them through an analytical model. Thus, we suppress them by focusing on dark matter haloes with masses inside a specific range. For the masses we use the definition of virial mass, $M_{200\rho_{\text{crit}}}$, which is the total mass contained within the virial radius of the halo, where the mean density is equal to 200 times the critical density of the universe at that time. In addition, we select only the dark matter particles that are gravitationally bound to them. We also further suppress filamentary structures by looking at slices of the simulation box with reduced thickness, Δz .

Finally, in order to generate more images from the L025N0376 simulation, we look at projected density maps of different subvolumes of the 25 Mpc cosmological box. Using the coordinates of the centers of potential (CoP) of the haloes, we select only those which belong to $12.5 \times 12.5 \times \Delta z$ Mpc³ subvolumes, where $\Delta z \in (8, 25)$ Mpc. For example, by choosing haloes with masses $M_{200\rho_{\text{crit}}} \in (10^9, 10^{12}) M_\odot$ and CoP's inside three different $12.5 \times 12.5 \times 12.5$ Mpc³ boxes of the L025N0376 simulation, we get different projections, in which the filamentary structure is suppressed (see Fig. 2).

2.2 Toy halo model

Next, we build a simple forward model consisting of four physical parameters, that generates images similar to the ones shown in Fig. 2. As mentioned in Section 2.1, those images are projected density maps of different sub-volumes of the 25Mpc cosmological box.

Therefore, the first parameter of our model is the number of haloes, N , that we will place on a projected plane. We sample halo masses from a halo mass function of the form

$$\frac{dn}{dM} = b \left(\frac{M}{M_\odot} \right)^{-a}, \quad (1)$$

(see e.g., Jenkins et al. 2001; Warren et al. 2006; Lukić et al. 2007; Tinker et al. 2008; Boylan-Kolchin et al. 2009) where a , the slope of the halo mass function, is the second parameter of our model. As further described in Appendix A, the sampling procedure does not depend on the normalization, b . Thus, b is not a parameter of our model.

Once we obtain the masses of the N haloes, we calculate their concentrations using the concentration-mass relation derived by Correa et al. (2015).

2.2.1 Spatial distribution

Next, we place the haloes on a projected plane. Since haloes in actual N-body simulation images are clustered, we mimic this behaviour by introducing correlations amongst the positions of different haloes. The most simple way to do it, in terms of computational speed and efficiency, is by using two-point correlation functions (or their Fourier transforms, power spectrums) and Gaussian fields, which are completely determined, in a statistical sense, by them. Therefore, we

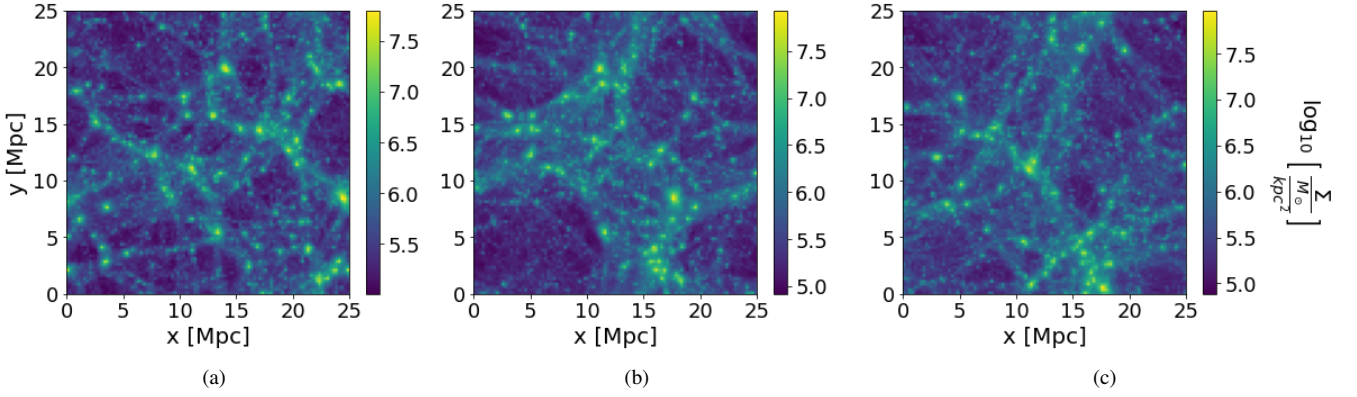


Figure 1. Logarithmic surface density of dark matter in units of $\frac{M_\odot}{\text{kpc}^2}$, calculated from two-dimensional histograms of the redshift-zero snapshot of a dark matter-only $(25 \text{ Mpc})^3$ simulation. In Fig. 1a, coordinate $z \in (0, 25) \text{ Mpc}$ is projected, while in Fig. 1b and Fig. 1c coordinates $y \in (0, 25) \text{ Mpc}$ and $x \in (0, 25) \text{ Mpc}$ are projected.

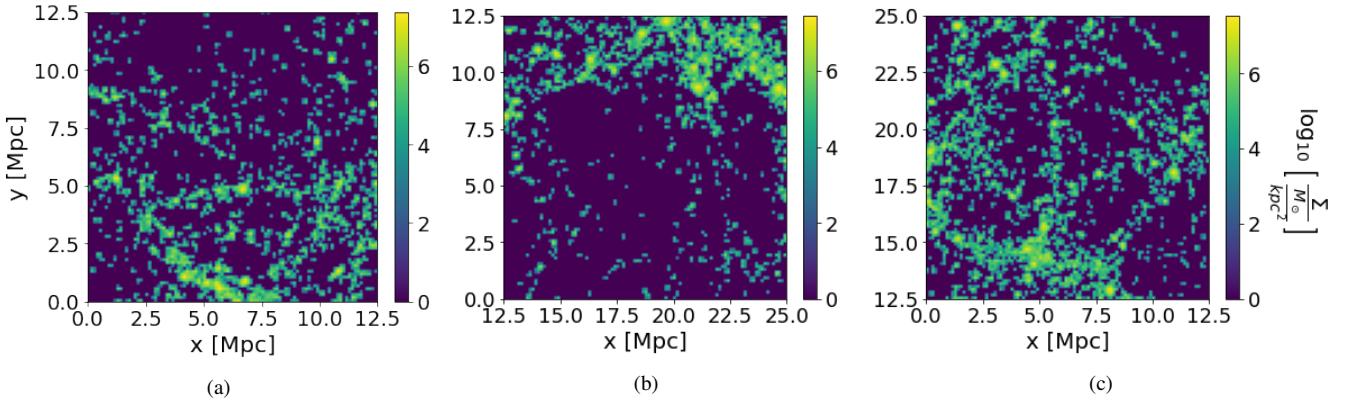


Figure 2. Logarithmic surface density of dark matter haloes in units of $\frac{M_\odot}{\text{kpc}^2}$, calculated from two-dimensional histograms of the redshift zero snapshot of the $(25 \text{ Mpc})^3$ simulation. These densities correspond to different $12.5 \times 12.5 \times 12.5 \text{ Mpc}^3$ sub-boxes of the simulation and to haloes with mass $M_{200\text{crit}} \in (10^9, 10^{12}) M_\odot$. In all images coordinate $z \in (0, 12.5) \text{ Mpc}$ is projected.

sample the positions of the haloes according to distributions generated from 2D realizations of Gaussian random fields on an $M \times M$ grid. In our case, the Gaussian field, δ_{ab}^x , is specified by a power spectrum given by a power-law

$$P(k) \sim \frac{1}{k^n}, \quad (2)$$

where n is the slope of the power spectrum, which is the third parameter of our model (for more details see Appendix B1 and Appendix B2).

Once we have the Gaussian field, δ_{ab}^x , we convert it into a probability distribution function, in order to be able to sample the positions of the haloes from it. To do that, we first multiply δ_{ab}^x with a parameter ϵ , which is the fourth parameter of our model. We calculate the field $f = e^{\epsilon \delta_{ab}^x}$ to get strictly positive values, and we normalize it so that its values sum to one. The role of the parameter ϵ is to further control the over and under densities in the Gaussian field produced by a given power spectrum. For example, $\epsilon=0$ will result in a uniform distribution, while a large ϵ will generate pronounced peaks. However, the parameter ϵ and the field δ_{ab}^x can be very correlated or degenerate. In order to reduce these effects, before exponentiating, we normalize the field δ_{ab}^x such as to have a constant variance, which is set to one.

Then, we use the normalized field f to sample the positions of

the haloes, and finally, we place each halo in the 2D plane. What we obtain are images where the values of their pixels correspond to the distance between the center of the pixel and a fixed reference which is the position of the halo, i.e., we obtain the projected radius, r' , of each halo. More details about the sampling of the positions of the haloes and the calculation of their projected radius, r' , can be found in Appendix B3.

Since we know the projected radius, r' , the mass, M_h , and the concentration, c , of each halo, we can use them to calculate the halo's surface density. We assume that haloes follow an NFW density profile (Navarro et al. 1997). The surface density of these haloes, in units of $\frac{M_\odot}{\text{kpc}^2}$ and in terms of the projected radius, r' , the scale radius, r_s and the concentration, c , is equal to

$$\begin{aligned} \rho_{2D}(r') &= \rho_c^0 \cdot \delta_{char} \cdot f_{2D}(r') \\ &= 277.5 h^2 \cdot \frac{200 c^3 g(c)}{3} \cdot f_{2D}(r'), \end{aligned} \quad (3)$$

where

$$g(c) = \frac{1}{\ln(1+c) - c/(1+c)}, \quad (4)$$

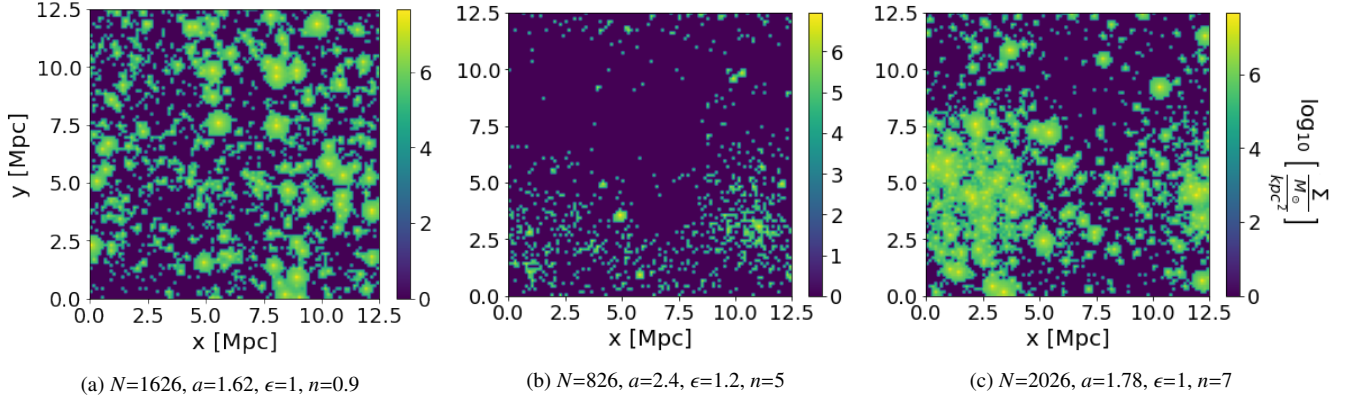


Figure 3. Logarithmic surface density of dark matter haloes with masses $M_h \in (10^9, 10^{12}) M_\odot$, in units of $\frac{M_\odot}{\text{kpc}^2}$. These images are mock data generated by the simple toy halo model described in Section 2.2, which contains four physical parameters and includes clustering. In each panel the parameters, i.e., the number of dark matter haloes (N), the slope of the halo mass function (a) and the parameters that control the clustering, namely the exponent multiplied with density field (ϵ) and the slope of the power spectrum (n), are randomly generated.

and $f_{2D}(r')$ is the 2D projection of the NFW profile

$$\rho(r) = \frac{\rho_c^0 \delta_{char}}{\left(\frac{r}{r_s}\right) \left(1 + \frac{r}{r_s}\right)^2}, \quad (5)$$

which is given by

$$f_{2D}(r') = -\frac{2r_s^3 \cdot \left[r' \cdot (r_s^2 - r'^2) + 2r_s \cdot r' \cdot \arctan\left(\frac{r' \cdot \sqrt{r_s^2 - r'^2}}{r' \cdot \sqrt{r_s^2 + r'^2}}\right) \cdot \sqrt{r'^2 - r_s^2} \right]}{r' \cdot (r_s^4 - 2r_s^2 \cdot r'^2 + r'^4)}. \quad (6)$$

This formula is derived analytically in Dimitriou (2021) and is equivalent to the one presented in Lokas & Mamon (2001). Using the definition of the halo concentration

$$c \equiv \frac{r_h}{r_s}, \quad (7)$$

and of the virial mass of a halo which follows an NFW profile,

$$M_h = \frac{4\pi}{3} 200 \rho_c^0 r_h^3, \quad (8)$$

we can express eq. (6) in terms of the mass, M_h , of the halo and its concentration, c , since

$$r_s = \frac{r_h}{c} = \frac{\left(\frac{3M_h}{4\pi\rho_c^0 200}\right)^{1/3}}{c} = \frac{(3M_h)^{1/3}}{(800\pi\rho_c^0)^{1/3} c}. \quad (9)$$

After calculating the surface density of a halo at all pixels, we set the values of the pixels that correspond to projected radii larger than $2.7 \cdot r_h$ equal to 1, where r_h is the halo's virial radius. In this way, we define an artificial boundary for each halo which depends on its mass, M_h . Once we calculate the \log_{10} of the pixels of these images, the regions after that boundary will be empty. We do that in order to be able to construct images similar to those of Fig. 2.

By adding images of multiple haloes together, we obtain the total surface density field, generated by the N haloes. Constructing the grids in the way that we described above, results in an image which has the same dimensions and pixel size as the ones of Fig. 2.

Finally, we add poisson noise to the image, since this is also the noise that actual N-body simulations have, due to their finite number of particles. The noisy image is obtained by sampling each of its pixels from a poisson distribution with λ equal to the value of the corresponding pixel of the noiseless image. Examples of images (mock data) generated from different combinations of the parameters of our model can be seen in Fig. 3.

2.3 Simulation-based inference

As described above, our forward model consists of a set of parameters, \mathbf{z} . The parameters \mathbf{z} are either physical parameters, denoted by θ , or latent nuisance variables denoted by ω , i.e., we have $\mathbf{z} = \theta \cup \omega$. The physical parameters are the number of haloes, N , the slope of the halo mass function, a , the exponent, ϵ , and the slope of the power spectrum, n . The latent nuisance variables are all the variables that are generated randomly in different parts of the model. Thus, more specifically, our model takes as input a vector of parameters θ , samples many internal states ω , and finally produces a data vector $\mathbf{x} \sim p(\mathbf{x}|\mathbf{z}) = p(\mathbf{x}|\theta, \omega)$.

Given the observed data \mathbf{x} , we want to infer the input parameters θ . Obtaining marginal posteriors of the parameters of interest using likelihood-based inference methods, involves evaluating the likelihood function $p(\mathbf{x}|\theta)$. However, this likelihood is defined implicitly by the forward model and often is not tractable, since it should be calculated by the high-dimensional integral

$$p(\mathbf{x}|\theta) = \int d\omega p(\mathbf{x}, \omega|\theta), \quad (10)$$

where $p(\mathbf{x}, \omega|\theta)$ is the joint probability density of data \mathbf{x} and of the very large latent space ω (Cranmer et al. 2020).

2.3.1 Neural Ratio Estimation (NRE)

One recently proposed likelihood-free inference technique is Neural Ratio Estimation (NRE) (Hermans et al. 2020). The goal of Ratio Estimation is to approximate the ratio

$$r(\mathbf{x}, \theta) \equiv \frac{p(\mathbf{x}, \theta)}{p(\mathbf{x})p(\theta)} = \frac{p(\mathbf{x}|\theta)}{p(\mathbf{x})} = \frac{p(\theta|\mathbf{x})}{p(\theta)}. \quad (11)$$

Given the prior $p(\theta)$ of the parameters, learning the ratio is enough in order to estimate the posterior $p(\theta|\mathbf{x})$. According to Hermans et al. (2020) it is possible to estimate this ratio by training a neural network (NN) as a parametrized binary classifier $d(\mathbf{x}, \theta)$ to distinguish dependent sample-parameter pairs $(\mathbf{x}, \theta) \sim p(\mathbf{x}, \theta)$ with class label $y = 1$ from independent sample-parameter pairs $(\mathbf{x}, \theta) \sim p(\mathbf{x})p(\theta)$ with class label $y = 0$.

We would like the output of the NN $d_\phi(\mathbf{x}, \theta)$, where ϕ are the network weights, to be interpreted as the probability of class with

label 1,

$$d_\phi(\mathbf{x}, \theta) = p(y = 1 | \mathbf{x}, \theta) = \quad (12)$$

$$\begin{aligned} &= \frac{p(\mathbf{x}, \theta | y = 1)p(y = 1)}{p(\mathbf{x}, \theta | y = 1)p(y = 1) + p(\mathbf{x}, \theta | y = 0)p(y = 0)} = \\ &= \frac{p(\mathbf{x}, \theta)}{p(\mathbf{x}, \theta) + p(\mathbf{x})p(y)}, \end{aligned} \quad (13)$$

assuming equal class population. Since we deal with a binary classifier, the binary-cross entropy loss function can be used in order to train the network via stochastic gradient descent. In the limit of infinite training data the loss functional is

$$\begin{aligned} L[d_\phi(\mathbf{x}, \theta)] \\ = \int d\theta \int d\mathbf{x} p(\mathbf{x}, \theta) [-\log d_\phi(\mathbf{x}, \theta)] + p(\theta) p(\mathbf{x}) [-\log(1 - d_\phi(\mathbf{x}, \theta))]. \end{aligned} \quad (14)$$

This loss functional is minimized exactly for the function $d_\phi(\mathbf{x}, \theta)$ defined at eq. (13), as described in Appendix C1.

After training the NN with a given number of training data, its output will be

$$d(\mathbf{x}, \theta) \approx \frac{p(\mathbf{x}, \theta)}{p(\mathbf{x}, \theta) + p(\mathbf{x})p(\theta)}. \quad (15)$$

By using eq. (15), we can estimate directly the posterior $p(\theta | \mathbf{x})$ as

$$p(\theta | \mathbf{x}) \approx \frac{d(\mathbf{x}, \theta)}{d(\mathbf{x}, \theta) - 1} p(\theta) = \hat{p}(\theta | \mathbf{x}), \quad (16)$$

(for more details see Appendix C2).

2.3.2 Marginal Neural Ratio Estimation (MNRE)

In order to obtain the marginal posteriors of the physical parameters, we will apply Marginal Neural Ratio Estimation (MNRE; Miller et al. 2021). MNRE is implemented via *swyft*¹ (Miller et al. 2020), an open-source software package, which estimates marginal likelihood-to-evidence ratios, that are amortized over a range of observational data \mathbf{x} and physical parameters θ .

According to this method, first we define the parameters of interest θ_k . The parameters θ_k include physical parameters of the model associated with all the one dimensional marginal posteriors such as $\{\theta_1, \theta_2, \theta_3, \theta_4\} = \{N, a, \epsilon, n\}$, parameters associated with all two dimensional marginal posteriors such as $\{(\theta_i, \theta_j) \in \mathbb{R}^2 | i = 1, \dots, 4, j = i + 1, \dots, 4\}$ and unions of these sets.

Swyft then uses NRE to estimate the corresponding marginal likelihood-to-evidence ratios

$$r_k(\mathbf{x}, \theta_k) := \frac{p(\mathbf{x} | \theta_k)}{p(\mathbf{x})} = \frac{p(\theta_k | \mathbf{x})}{p(\theta_k)}. \quad (17)$$

More details can be found in Appendix C3.

2.4 Training

In order to start training binary classifiers to get marginal posteriors of the physical parameters of our model, we first define the priors of the parameters and the number of training data. These parameters, together with their priors, can be seen in Table 1.

Moreover, we choose to train with 200,000 mock data samples and we define a preprocessor network that acts as feature extractor: a Convolutional Neural Network (CNN), whose architecture can be seen in Fig. 4. We train using a batch size of 64, a learning rate of 10^{-4} and for a maximum of 100 epochs.

Table 1. The physical parameters of the toy halo model described in Section 2.2 together with their uniform priors used during training.

Parameter	Range
N : Number of haloes	100-2000
a : Inner slope of halo mass function	1-3
ϵ : Exponent of the Gaussian random field	0-2
n : Slope of the power spectrum	0-10

3 RESULTS

This Section is structured as follows. In Section 3.1 we evaluate the performance of the trained NN on mock data. In Section 3.2, we test its performance on N-body simulation data. More specifically, in Section 3.2.1 we focus on reconstructing the halo mass function, while in Section 3.2.2 on estimating the lowest mass of the haloes, or alternatively, an artificial lowest cutoff of the halo mass function of the N-body simulation images.

3.1 Inference of simulation model

Examples of the resulting one dimensional posteriors of the parameters of two mock images, together with their correct values and their highest posterior density regions, can be seen in Fig. 5. The figure shows that the NN is able to reconstruct the four parameters since their correct values (vertical dashed lines) lie inside the 1σ and 2σ intervals of their corresponding posteriors.

To test the performance of the trained NN, and therefore the quality of the posteriors and their credible regions, we use mock data and the notions of the nominal and empirical expected coverage probabilities. Following Hermans et al. (2021a), the empirical expected coverage probability of the $1 - \alpha$ highest posterior density regions, derived from the posterior estimator $\hat{p}(\theta_k | \mathbf{x})$, given a set of n i.i.d. mock data $(\theta_{ki}^*, \mathbf{x}_i) \sim p(\theta_k, \mathbf{x})$, can be calculated as

$$1 - \hat{\alpha} = \frac{1}{n} \sum_{i=1}^n \mathbb{1}[\theta_{ki}^* \in \Theta_{\hat{p}(\theta_k | \mathbf{x}_i)}(1 - \alpha)]. \quad (18)$$

In this expression $\Theta_{\hat{p}(\theta_k | \mathbf{x})}(1 - \alpha)$ is the $1 - \alpha$ highest posterior density region of $\hat{p}(\theta_k | \mathbf{x})$ and θ_{ki}^* is the ground truth specified to the simulation model, whose forward evaluation produced the observable \mathbf{x} . On the other hand, the nominal expected coverage probability is the expected coverage probability of the true posterior and is equal to the confidence level $1 - \alpha$. Therefore, this expression allows us to estimate the actual error rate $\hat{\alpha}$ of a $1 - \alpha$ highest posterior density region of $\hat{p}(\theta_k | \mathbf{x})$. In the case of a perfectly calibrated posterior the empirical expected coverage probability is equal to the nominal expected coverage probability. This means that when we randomly generate observations $(\mathbf{x}, \theta_k) \sim p(\mathbf{x} | \theta_k)p(\theta_k)$, we expect the true parameters θ_k^* to fall outside of the $1 - \alpha$ region in α of the cases (Cole et al. 2021). According to Hermans et al. (2021a), a posterior estimator is considered to be acceptable whenever the empirical expected coverage probability is larger or equal to the nominal expected coverage probability.

Fig. 6 highlights our results. In these panels we reparametrize α ($\hat{\alpha}$) with a new variable z (\hat{z}), defined as the $1 - \frac{1}{2}\alpha$ ($1 - \frac{1}{2}\hat{\alpha}$) quantile of the standard normal distribution, following Cole et al. (2021). Therefore, the most commonly used “ 1σ ”, “ 2σ ” and “ 3σ ” regions that correspond to $1 - \alpha = 0.6827, 0.9545, 0.9997$ are quoted as $z = 1, 2, 3$. Furthermore, we denote the empirical coverage in terms of $1 - \hat{\alpha}$ (horizontal numbers) for the above mentioned confidence

¹ <https://github.com/undark-lab/swyft>

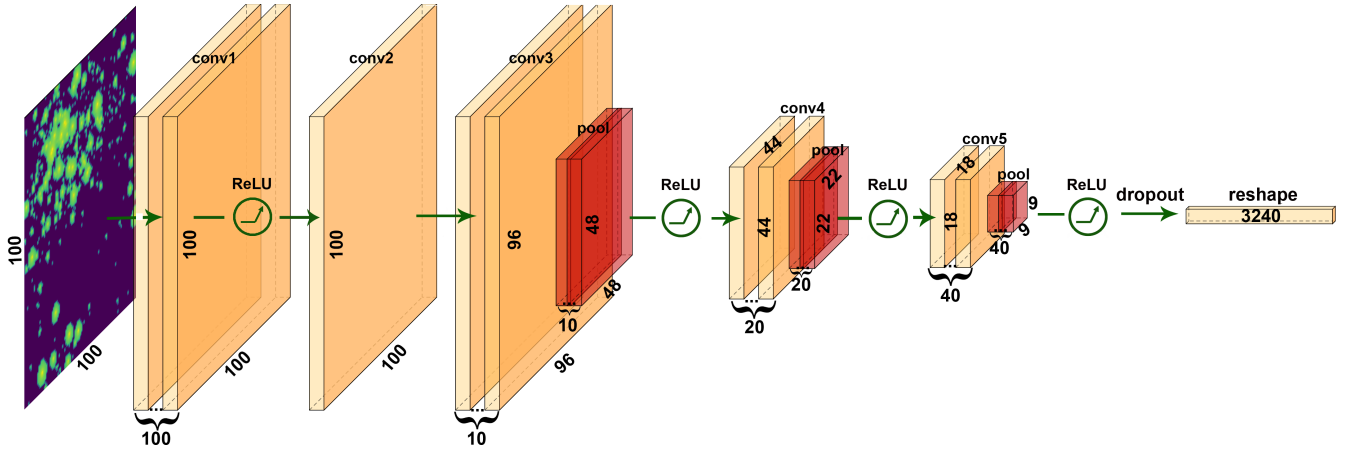


Figure 4. The CNN used to preprocess the mock data produced by the toy halo model described in Section 2.2. The CNN consists of 13 layers: conv1 → ReLU → conv2 → conv3 → max-pool → ReLU → conv4 → max-pool → ReLU → conv5 → max-pool → ReLU → dropout. After the final dropout layer, the data are reshaped into a 1D array which is the input for an MLP, as described in Section 2.3.2.

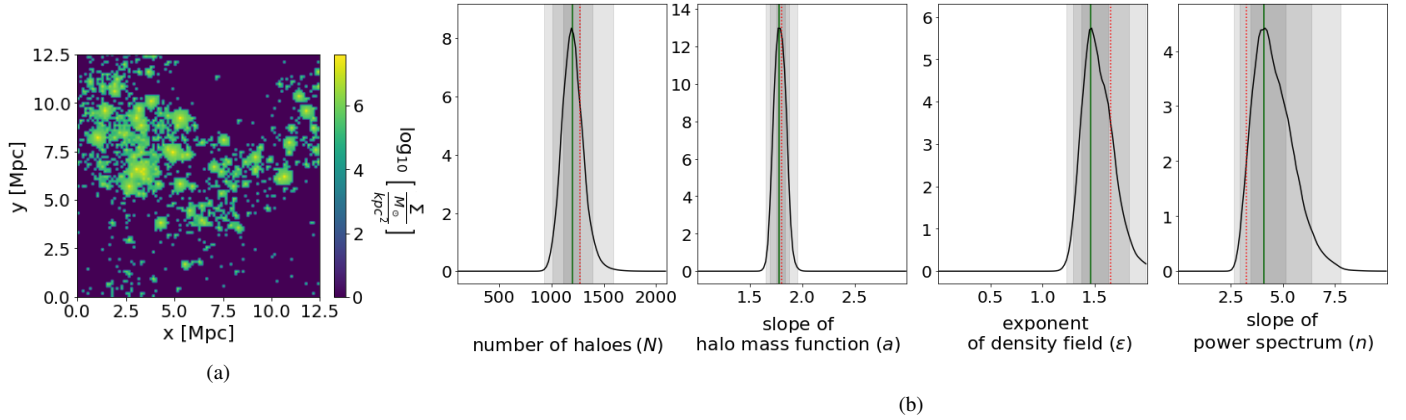


Figure 5. Fig. 5a is generated from the toy halo model described in Section 2.2, using $N=1253$, $a=1.78$, $\epsilon=1.64$ and $n=3.21$ and depicts the logarithmic surface density of dark matter haloes with masses $M_h \in (10^9, 10^{12}) M_\odot$, in units of $\frac{M_\odot}{\text{kpc}^2}$. Fig. 5b illustrates the one dimensional marginal posteriors for the four physical parameters of the toy halo model. The correct values of the parameters (vertical red dashed lines), the modes of the posteriors (vertical green lines) and their 68.72%, 95.45% and 99.73% highest posterior density regions (grey regions) can be seen.

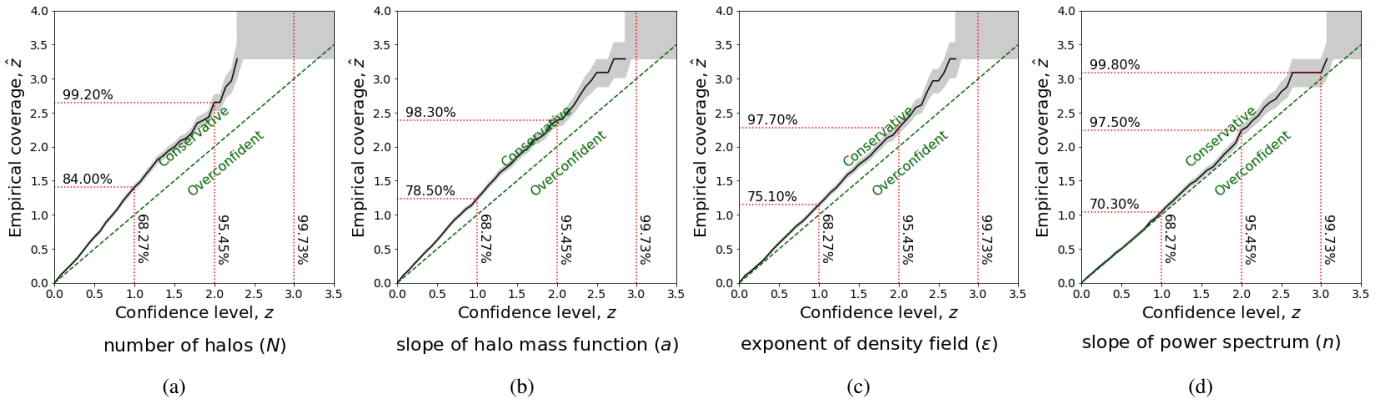


Figure 6. Empirical expected coverage probability as function of the confidence level, $1 - \alpha$, or alternatively of z , for the four physical parameters of the toy halo model described in Section 2.2. The probabilities are calculated using simulation data. In cases where $\hat{z} > z$, the estimated credible intervals are conservative and contain the true values with a frequency higher than nominally expected. The nominal probabilities $1 - \alpha$ are shown in vertical dashed red lines, while the empirical estimates $1 - \hat{\alpha}$ are shown in the horizontal ones.

levels (vertical numbers). Finally, we estimate uncertainties of the expected coverage probability due to the finite total number of mock data, n , using Jeffreys interval (Cole et al. 2021).

By looking at Fig. 6, we see that the 68.27% (95.45%) highest posterior density region corresponding to parameter N , contains the ground truth value in 84.00% (99.20%) of the cases, and is hence conservative, or in other words the confidence intervals over-cover. In the case of perfect coverage, one would expect the black and the green dashed line to perfectly overlap. Moreover, we observe that the highest posterior density regions corresponding to parameters a , ϵ and n , are slightly conservative too. Therefore, following Hermans et al. (2021a), our posterior estimators are conservative.

3.2 N-body simulation images

Now, we can test the NN's performance on actual N-body simulation images, like those of Fig. 2. At first, we will test if the NN is able to reconstruct the halo mass function.

3.2.1 Reconstructing the halo mass function

As opposed to mock images, in the case of N-body simulations, only two of the correct values of the parameters are known: the number, N , of the haloes in each image, which can be calculated by using the data provided by the FOF halo finder and the slope, a , of the halo mass function, which is found to be ~ 1.9 (Zavala & Frenk 2019). Thus, we would like to see whether the NN is able to reconstruct the halo mass function, i.e., if it is able to identify the correct values of N and a and also to predict the values of the clustering parameters ϵ and n for sub-boxes of the simulation L025N0376, like those of Fig. 2. To increase the size of our test data set we also rotate each sub-box by 90, 180 and 270 degrees. The highest posterior density regions that correspond to 16 sub-boxes, together with the correct values of the parameters N and a , can be seen in Fig. 8.

By looking at this figure, we see that the NN estimates correctly the number of haloes of all images, since the correct values of N lie either inside the 68.45% (1σ) or the 94.74% (2σ) highest posterior density regions. The same holds also for the inner slope, a , of the halo mass function. Moreover, we see that the posteriors of the slope, n , of the power spectrum are narrow, while the posteriors for the parameter ϵ are wide.

Since the posteriors of ϵ are wide and they overlap, i.e., ϵ is not very constrained, we can calculate a combined posterior. We can do the same also for a and n , since their posteriors are narrow and do not vary a lot between the different images. The combined posteriors of the above mentioned parameters are calculated using the 16 N-body simulation images, which we treat as a set of independent and identically distributed data (i.i.d) $\mathcal{X} = \{x_1, \dots, x_{16}\}$ ². Following Hermans et al. (2020), these posteriors are equal to

$$p_{comb}(\vartheta|\mathcal{X}) = \frac{p(\vartheta) \prod_{x \in \mathcal{X}} p(x|\vartheta)}{\int p(\vartheta) \prod_{x \in \mathcal{X}} p(x|\vartheta) d\vartheta} \sim \frac{p(\vartheta) \prod_{x \in \mathcal{X}} \hat{p}(x, \vartheta)}{\int p(\vartheta) \prod_{x \in \mathcal{X}} \hat{p}(x, \vartheta) d\vartheta}, \quad (19)$$

where $\vartheta \in \{a, \epsilon, n\}$. The combined posteriors of the parameters a , ϵ and n that we obtain can be seen in Fig. 9.

² In fact, not all images are exactly independent from each other. As already mentioned, some of them are obtained by rotating others by 90, 180 and 270 degrees.

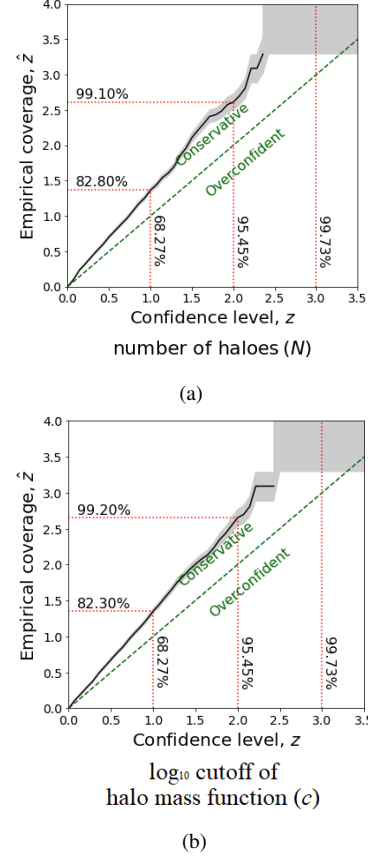


Figure 7. Like Fig. 6, but for the parameters N and c of the toy halo model described in Section 3.2.2.

Below we will generate mock images by letting the parameter N vary, while we will set the values of a , ϵ and n equal to the modes of these combined posteriors. A comparison between those mock images and images of Fig. 2 in pixel space, can be found in Appendix E.

3.2.2 Reconstructing the lower cutoff of the halo mass function

Now, we will test if we can identify the lowest mass of the haloes in the N-body simulation images. To this end, we first need to modify the model described in Section 2.2.

Up to now, we were always sampling haloes with masses $M_h \in (10^9, 10^{12}) M_\odot$ according to the PDF of the halo mass function (more details about this can be found in Appendix A). In order to be able to sample haloes with masses $M_h \in (10^c, 10^{12}) M_\odot$, where c is a new parameter, we will replace that PDF, with a new one defined as

$$\text{PDF}_c(M) = \frac{(1-a)}{(10^{12})^{1-a} - (10^c)^{1-a}} \cdot \left(\frac{M}{M_\odot}\right)^{-a}. \quad (20)$$

In this way we add an artificial lower cutoff in the halo mass function of eq. (1). Moreover, we will utilize the results of Section 3.2.1 and therefore we will set the values of the parameters a , ϵ and n equal to the modes of their combined posteriors, i.e., $a=1.9025$, $\epsilon = 1.5675$ and $n=2.0375$. Thus the new model has only two parameters: the number, N , of haloes and the cutoff, c , of the halo mass function.

After defining the new model, we train a NN as before, but since we have only two parameters, we train with 50.000 mock data. The parameters, together with their priors are shown in Table 2. To ensure that the trained NN performs well, we perform a coverage test

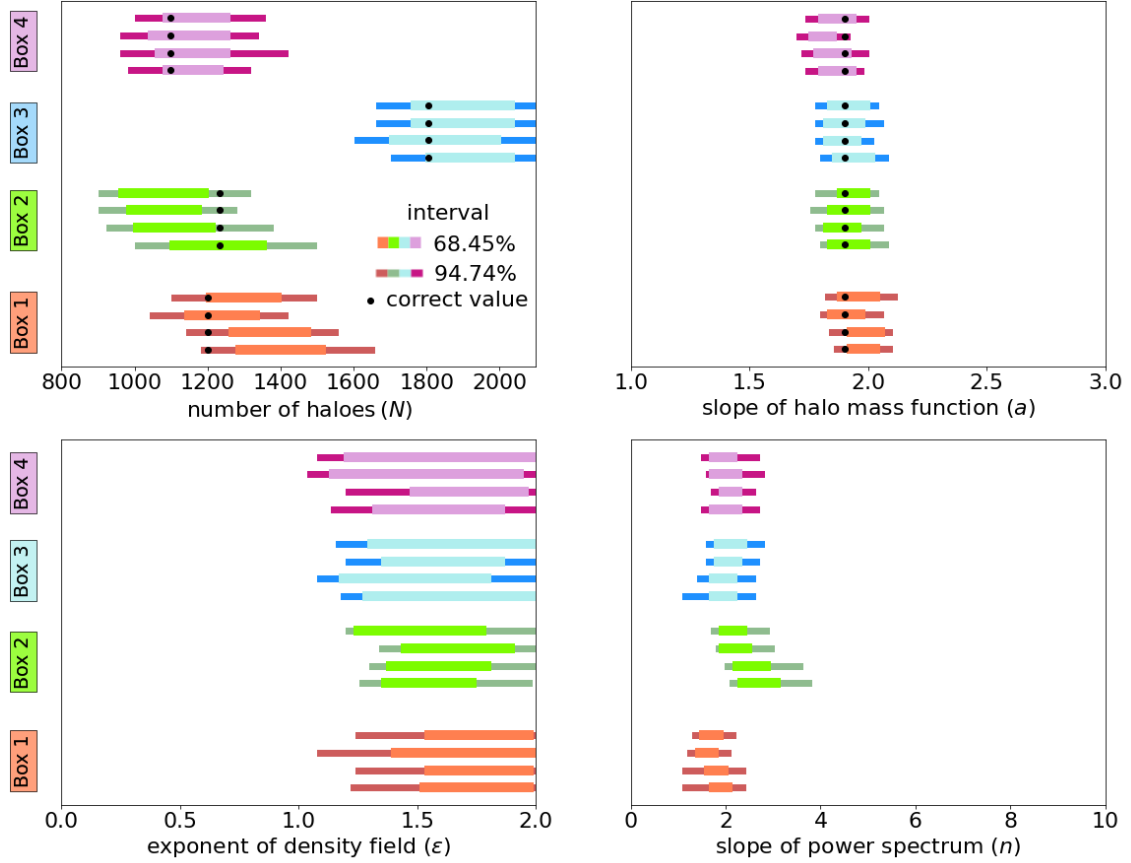


Figure 8. (Main Result 1) 68.45% and 94.74 % highest posterior density regions of the four physical parameters of a simple toy halo model that includes clustering, which is directly derived from dark-matter-only simulations using Marginal Neural Ratio Estimation (MNRE). Each color corresponds to results obtained by a sub-box of a $(25 \text{ Mpc})^3$ simulation and three rotations of it, for which we know the correct values for the number of haloes, N , and the slope of halo mass function, a . We reproduce the number of haloes and the slope of halo mass function reasonably well (the correct values lie inside the 1σ and 2σ intervals), while we predict the values of ϵ and n which are effective parameters of a clustering model that is based on a toy implementation of two-body correlation functions. We also observe that the results obtained by each sub-box and the three rotations are very stable, despite the fact that rotations change the images completely.

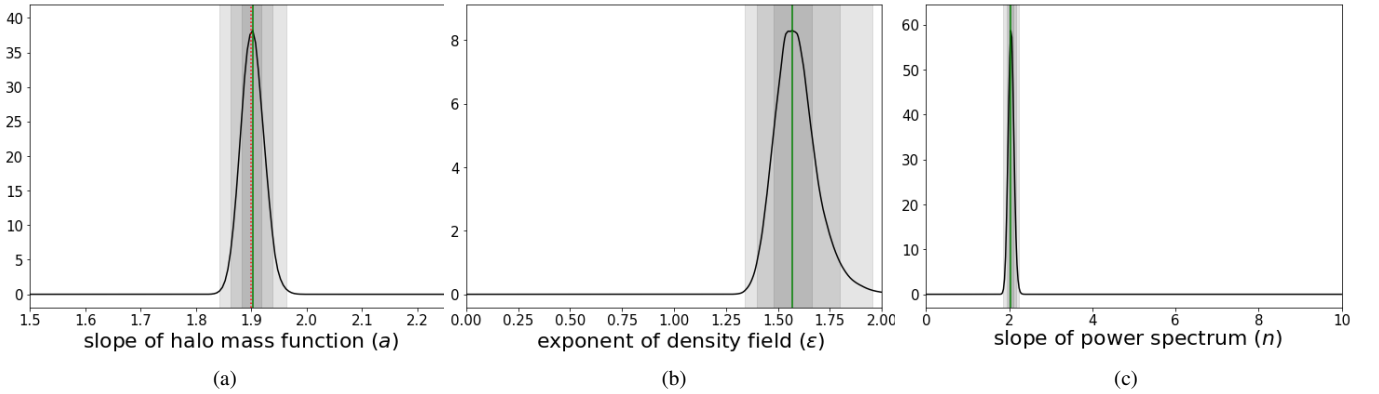


Figure 9. Combined posteriors of the parameters a , ϵ and n of the toy halo model described in Section 2.2, along with their modes (green lines), their 68.45%, 94.74% and 99.73% highest posterior density regions and the correct value of the parameter a (red dashed line). The combined posterior of each parameter is calculated using the results of Fig. 8 which are obtained by a set of independent and identically distributed N-body simulation images, according to eq. (19). We manage to reconstruct the slope of the halo mass function since its correct value, 1.9, lies inside the 1σ interval of the combined posterior.

Table 2. The physical parameters of the toy halo model described in Section 3.2.2 together with the uniform priors used during training.

Parameter	Range
N : Number of haloes	100-3000
c : \log_{10} lower cutoff of halo mass function	8-10.5

similar to that of Section 3.1. By looking at Fig. 7, we see that the 68.27% and 95.45% highest posterior density regions corresponding to both parameters N and c , are slightly conservative. Since our posterior estimators are conservative under the simulation model, we can test the NN's performance on actual N-body simulation images, like those of Fig. 10. These images correspond to \log_{10} surface densities produced by haloes with masses $M_h \in (10^c, 10^{12}) M_\odot$ where $c \in \{8.75, 9, 9.5\} M_\odot$. We choose to generate images in these mass ranges, since smaller cutoffs, e.g. $c=8 M_\odot$, are inside the resolution limit of the simulations, while larger cutoffs, e.g. $c=10 M_\odot$, result in images with very few haloes.

The results that be obtain can be seen in Fig. 11. We see that the NN is able to identify the correct values of the \log_{10} cutoff, c , since they always lie inside the 1σ or 2σ intervals. In most cases, the same holds for the number of haloes, N , while sometimes our results are problematic, i.e., the 1σ or 2σ intervals do not contain the correct value of the parameter, especially when looking at images with many haloes that are very clustered, e.g., at Box 2 with $c = 8.75 M_\odot$. The image that corresponds to the same Box with $c = 9 M_\odot$ can be seen in Fig. 2b. By reducing the cutoff, the number of haloes increases and all of them are accumulated in the same region. In this case, we see that the NN underestimates the number of haloes. This behaviour can be explained by the fact that the new model has only two parameters, while the values of the parameters ϵ and n , which controlled the clustering at the four-parameter model, were set equal to the modes of their combined posteriors. These modes were calculated from 16 different images that had a specific amount of clustering. Therefore, our training data does not contain many images with few haloes which are almost uniformly distributed or images with many haloes that are all accumulated to a specific region. Thus, we conclude that our NN performs well on actual N-body simulations which have approximately the same amount of clustering with our training data, and it is able to identify the correct artificial lower cutoff of the halo mass function.

Finally, we can generate mock images which have the same number of haloes and cutoff with N-body simulation images, and compare them in pixel space. More details about this can be found in Appendix E.

4 CONCLUSIONS

In this work, we have shown how a simple analytical toy halo model can be used together with the likelihood-free inference technique Marginal Neural Ratio Estimation (MNRE), to infer parameters of dark matter-only cosmological simulations. Our toy model consists of a large number of parameters related to the halo mass function and to the spatial distribution of dark matter haloes. Such spatial distribution is generated from 2D realizations of Gaussian random fields determined by a power-law power spectrum. Most of the parameters of the model are nuisance latent variables that correspond to random samples from various distributions, while only four are kept explicitly: the number, N , of the dark matter haloes, the slope,

a , of the halo mass function and the parameters n, ϵ of our effective clustering model.

By applying MNRE³, we trained several neural networks with mock images generated by our model, to identify the correct values of the physical parameters that produced a given image. We showed that by using the trained neural networks on dark-matter-only simulation images and rotations of them, it is possible to achieve several key goals.

First, as illustrated in Fig. 8, we managed to reconstruct the halo mass function of those images, i.e., the number, N , of the haloes and the inner slope, a , of the halo mass function, reasonably well, as the correct values of those parameters always lie inside the 1σ and 2σ intervals. Moreover, as shown in Fig. 11, we were able to identify correctly the lowest mass of the haloes, i.e., the \log_{10} cutoff, c , of the halo mass function, while there were some deficiencies in reconstructing the number of haloes, especially when looking at images where the haloes were more clustered than those in our training data (see Box 2 of Fig. 11 and Section 3.2.2 for details). This behaviour is related to the fact that the clustering model that we use is ad-hoc and indicates a direction of future improvement. Furthermore, we observed the surprising fact that the results obtained by each image and its three rotations in both Fig. 8 and Fig. 11 are very stable, despite the fact that rotations change the images completely. Finally, as shown in Fig. E1 and Fig. E2, we were able to generate mock images which look similar to dark-matter-only simulations.

Despite the fact that our results are promising, we note that our model is not perfect and certainly, there are aspects of it that need improvement and refinement. As mentioned above, the model that we use to describe the clustering of the haloes, is an effective model, and apart from the fact that is physically motivated, it does not account for higher order correlations between the haloes. Therefore, we restricted our analysis to massive haloes, i.e., to haloes whose clustering can be approximated by a Gaussian field with a power-law power spectrum. However, in order to have a model which is completely physical and can also be used to produce filamentary structures, non-Gaussian features should be introduced. This is a non-trivial task, but previous works in which the nonlinear large-scale structure of the Universe is predicted by deep neural networks using the Zel'dovich approximation (He et al. 2019) or even using normalizing flows (Rouhiainen et al. 2021) could be used. Another direction of future improvement could be that of the refinement of the algorithm defining our simulator, by finding and easing its bottlenecks. Now, approximately one second is needed to construct an image with 2000 haloes. That means that generating thousands of mock images is feasible but time consuming. Moreover, using a more complicated model for clustering as suggested above, will probably result in a slowdown of the simulator. Therefore, attention should be given at the optimization of our code.

³ through the open-source code *swyft*

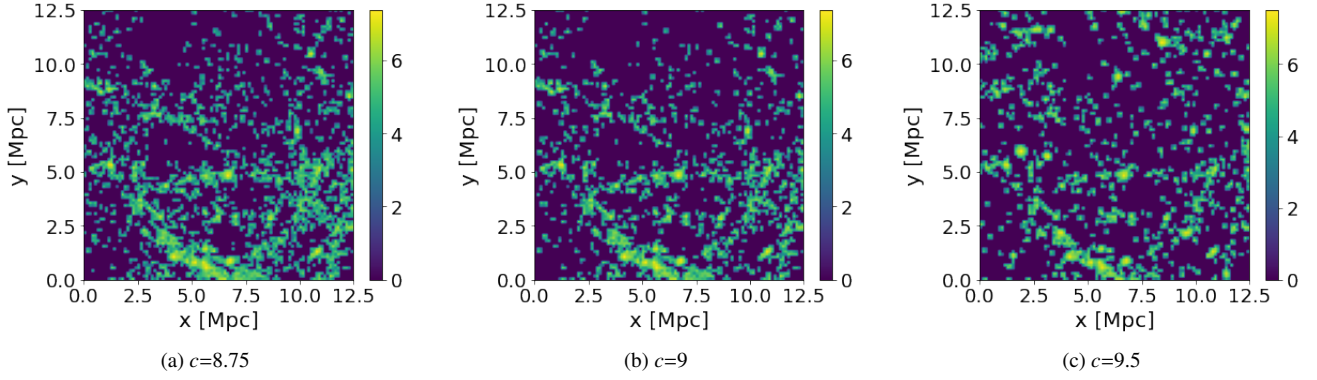


Figure 10. Logarithmic surface densities of dark matter haloes in units of $\frac{M_{\odot}}{\text{kpc}^2}$, calculated from two-dimensional histograms of the redshift zero snapshot of a $(25 \text{ Mpc})^3$ simulation. All images correspond to a single sub-box of the simulation, but they are generated using a different \log_{10} cutoff, c , of the halo mass function. The left panel shows the distribution of haloes more massive than $10^{8.75} M_{\odot}$, whereas the middle and right panels show the distribution of haloes more massive than 10^9 and $10^{9.5} M_{\odot}$ respectively.

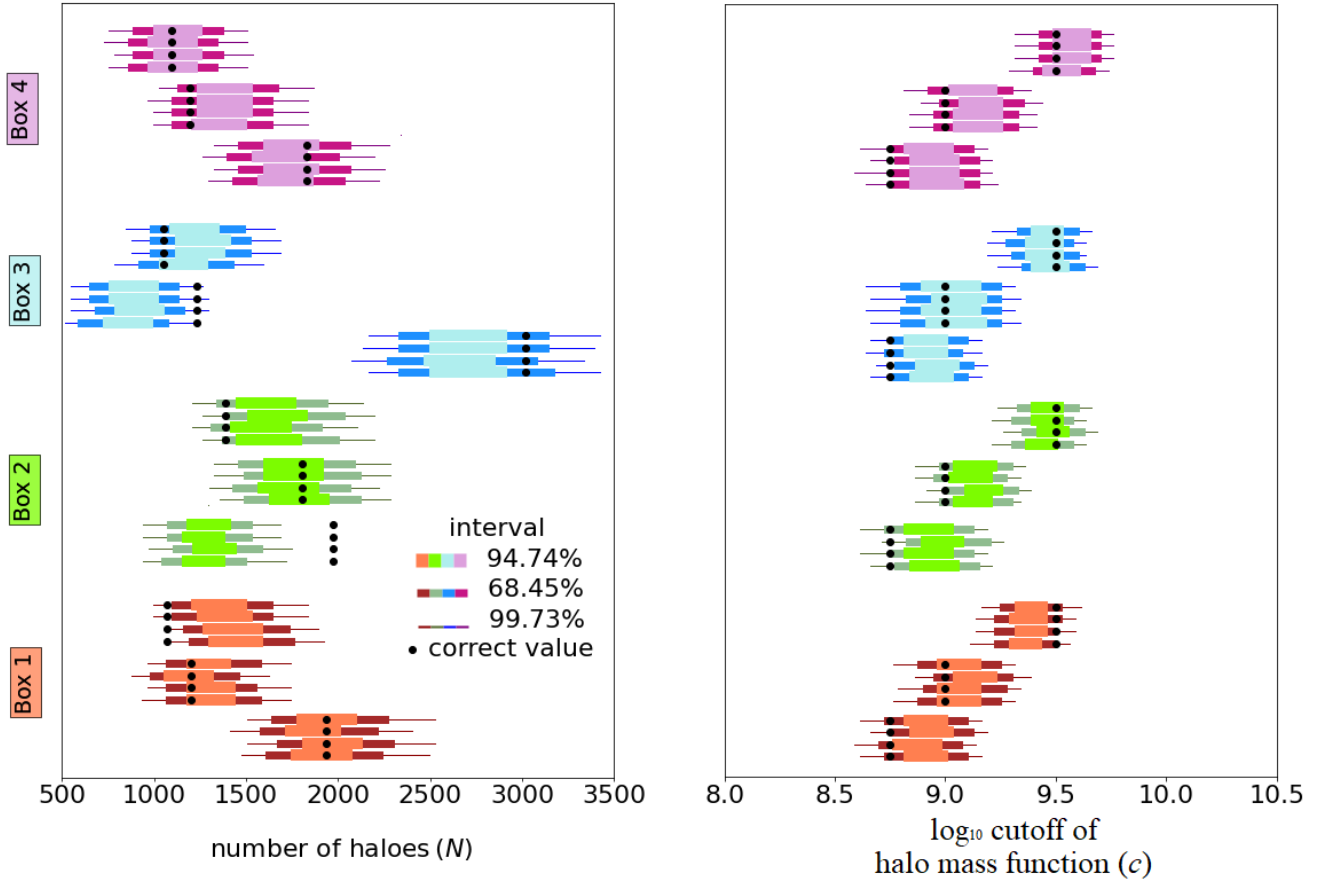


Figure 11. (Main Result 2) 68.45%, 94.74 % and 99.73% highest posterior density regions of the two physical parameters of the toy halo model described in Section 3.2.2, which is directly calibrated on dark-matter-only simulations using Marginal Neural Ratio Estimation (MNRE). Each color corresponds to a sub-box of a $(25 \text{ Mpc})^3$ simulation and 3 rotations of it. To construct this model we first use the results shown in Fig. 8 and we set the values of the three out of the four parameters (a , ϵ and n) of the simple toy halo model of Section 2.2, equal to the modes of their combined posteriors shown in Fig. 9. We also add a new parameter, c , which controls the lowest mass of the haloes in the simulations, i.e., it acts as a lower cutoff of the halo mass function. We manage to reproduce the logarithmic cutoff reasonably well since the correct values almost always belong in the 1σ and 2σ intervals. While in most cases the same holds for the number of haloes, we observe some deficiencies, especially when looking at images with many haloes that are very clustered (see e.g., Box 2 with $c=8.75 M_{\odot}$). As described in Section 3.2.2, these deficiencies result from the definition of the clustering in the toy halo model. Finally, we observe again that the results obtained by each sub-box and the three rotations are very stable, despite the fact that rotations change the images completely.

ACKNOWLEDGEMENTS

This work is part of a project that has received funding from the European Research Council (ERC) under the European Union's Horizon 2020 research and innovation programme (Grant agreement No. 864035). CAC acknowledges the support by the Dutch Research Council (NWO Veni 192.020). This work was carried out on the Dutch national e-infrastructures, Snellius and Lisa Cluster, with the support of SURF Cooperative. We acknowledge the use of the Python (Van Rossum & Drake 2009) modules, matplotlib (Hunter 2007), NumPy (Harris et al. 2020), SciPy (Virtanen et al. 2020), PyTorch (Paszke et al. 2019), tqdm (da Costa-Luis et al. 2021), and Jupyter (Kluyver et al. 2016).

DATA AVAILABILITY

The EAGLE data used in this article is available at <http://virgodb.dur.ac.uk/> (McAlpine et al. 2016; The EAGLE team 2017).

REFERENCES

- Abazajian K. N., et al., 2009, *ApJS*, **182**, 543
- Agarwal S., Davé R., Bassett B. A., 2018, *MNRAS*, **478**, 3410
- Alsing J., Wandelt B., Feeney S., 2018, *MNRAS*, **477**, 2874
- Alsing J., Charnock T., Feeney S., Wandelt B., 2019, *MNRAS*, **488**, 4440
- Alves de Oliveira R., Li Y., Villaescusa-Navarro F., Ho S., Spergel D. N., 2020, arXiv e-prints, p. [arXiv:2012.00240](https://arxiv.org/abs/2012.00240)
- Anau Montel N., Coogan A., Correa C., Karchev K., Weniger C., 2022, arXiv e-prints, p. [arXiv:2205.09126](https://arxiv.org/abs/2205.09126)
- Aragon-Calvo M. A., 2019, *MNRAS*, **484**, 5771
- Arjona R., Nesseris S., 2020, *Phys. Rev. D*, **101**, 123525
- Beck M. R., et al., 2018, *MNRAS*, **476**, 5516
- Behroozi P. S., Wechsler R. H., Conroy C., 2013, *ApJ*, **770**, 57
- Berger P., Stein G., 2019, *MNRAS*, **482**, 2861
- Birrer S., Amara A., Refregier A., 2017, *J. Cosmology Astropart. Phys.*, **2017**, 037
- Bond J. R., Cole S., Efstathiou G., Kaiser N., 1991, *ApJ*, **379**, 440
- Boylan-Kolchin M., Springel V., White S. D. M., Jenkins A., Lemson G., 2009, *MNRAS*, **398**, 1150
- Brehmer J., Mishra-Sharma S., Hermans J., Louppe G., Cranmer K., 2019, *ApJ*, **886**, 49
- Buck T., Wolf S., 2021, arXiv e-prints, p. [arXiv:2111.01154](https://arxiv.org/abs/2111.01154)
- Cole A., Miller B. K., Witte S. J., Cai M. X., Grootes M. W., Nattino F., Weniger C., 2021, arXiv e-prints, p. [arXiv:2111.08030](https://arxiv.org/abs/2111.08030)
- Coogan A., Karchev K., Weniger C., 2020, arXiv e-prints, p. [arXiv:2010.07032](https://arxiv.org/abs/2010.07032)
- Correa C. A., Wyithe J. S. B., Schaye J., Duffy A. R., 2015, *MNRAS*, **452**, 1217
- Cranmer K., Brehmer J., Louppe G., 2020, *Proceedings of the National Academy of Science*, **117**, 30055
- DESI Collaboration et al., 2016, arXiv e-prints, p. [arXiv:1611.00036](https://arxiv.org/abs/1611.00036)
- Dark Energy Survey Collaboration et al., 2016, *MNRAS*, **460**, 1270
- Dawson J. M., Davis T. A., Gomez E. L., Schock J., Zabel N., Williams T. G., 2020, *MNRAS*, **491**, 2506
- Dax M., Green S. R., Gair J., Macke J. H., Buonanno A., Schölkopf B., 2021, *Phys. Rev. Lett.*, **127**, 241103
- Delaunoy A., Wehenkel A., Hinderer T., Nissanke S., Weniger C., Williamson A. R., Louppe G., 2020, arXiv e-prints, p. [arXiv:2010.12931](https://arxiv.org/abs/2010.12931)
- Devroye L., 1986, *Non-Uniform Random Variate Generation*. Springer-Verlag, New York, NY, USA
- Dieleman S., Willett K. W., Dambre J., 2015, *MNRAS*, **450**, 1441
- Dimitriou A., 2021, Master's thesis, University of Amsterdam, <https://scripts.uba.uva.nl/search?id=723799>
- Dubois Y., Peirani S., Pichon C., Devriendt J., Gavazzi R., Welker C., Volonteri M., 2016, *MNRAS*, **463**, 3948
- Harris C. R., et al., 2020, *Nature*, **585**, 357
- He S., Li Y., Feng Y., Ho S., Ravanbakhsh S., Chen W., Póczos B., 2019, *Proceedings of the National Academy of Science*, **116**, 13825
- He Q., et al., 2022, *MNRAS*, **511**, 3046
- Hermans J., Begy V., Louppe G., 2020, in III H. D., Singh A., eds, *Proceedings of Machine Learning Research* Vol. 119, *Proceedings of the 37th International Conference on Machine Learning*. PMLR, pp 4239–4248, <https://proceedings.mlr.press/v119/hermans20a.html>
- Hermans J., Delaunoy A., Rozet F., Wehenkel A., Louppe G., 2021a, arXiv e-prints, p. [arXiv:2110.06581](https://arxiv.org/abs/2110.06581)
- Hermans J., Banik N., Weniger C., Bertone G., Louppe G., 2021b, *MNRAS*, **507**, 1999
- Hocking A., Geach J. E., Sun Y., Davey N., 2018, *MNRAS*, **473**, 1108
- Hunter J. D., 2007, *Computing in Science & Engineering*, **9**, 90
- Ivezić Ž., et al., 2019, *ApJ*, **873**, 111
- Jenkins A., Frenk C. S., White S. D. M., Colberg J. M., Cole S., Evrard A. E., Couchman H. M. P., Yoshida N., 2001, *MNRAS*, **321**, 372
- Karchev K., Coogan A., Weniger C., 2022, *MNRAS*, **512**, 661
- Khandai N., Di Matteo T., Croft R., Wilkins S., Feng Y., Tucker E., DeGraf C., Liu M.-S., 2015, *MNRAS*, **450**, 1349
- Kluyver T., et al., 2016, in Loizides F., Schmidt B., eds, *Positioning and Power in Academic Publishing: Players, Agents and Agendas*. pp 87 – 90
- LSST Science Collaboration et al., 2009, arXiv e-prints, p. [arXiv:0912.0201](https://arxiv.org/abs/0912.0201)
- Łokas E. L., Mamon G. A., 2001, *MNRAS*, **321**, 155
- Lovell C. C., Wilkins S. M., Thomas P. A., Schaller M., Baugh C. M., Fabian G., Bahé Y., 2021, *Monthly Notices of the Royal Astronomical Society*, **509**, 5046
- Lucie-Smith L., Peiris H. V., Pontzen A., Lochner M., 2018, *MNRAS*, **479**, 3405
- Lukić Z., Heitmann K., Habib S., Bashinsky S., Ricker P. M., 2007, *ApJ*, **671**, 1160
- Makinen T. L., Charnock T., Alsing J., Wandelt B. D., 2021, *J. Cosmology Astropart. Phys.*, **2021**, 049
- McAlpine S., et al., 2016, *Astronomy and Computing*, **15**, 72
- Miller B. K., Cole A., Louppe G., Weniger C., 2020, arXiv e-prints, p. [arXiv:2011.13951](https://arxiv.org/abs/2011.13951)
- Miller B. K., Cole A., Forré P., Louppe G., Weniger C., 2021, arXiv e-prints, p. [arXiv:2107.01214](https://arxiv.org/abs/2107.01214)
- Mo H. J., White S. D. M., 1996, *MNRAS*, **282**, 347
- Moews B., Davé R., Mitra S., Hassan S., Cui W., 2021, *MNRAS*, **504**, 4024
- Murray S. G., 2018, *Journal of Open Source Software*, **3**, 850
- Navarro J. F., Frenk C. S., White S. D. M., 1997, *ApJ*, **490**, 493
- Ntampaka M., Eisenstein D. J., Yuan S., Garrison L. H., 2020, *The Astrophysical Journal*, **889**, 151
- Paszke A., et al., 2019, in , *Advances in Neural Information Processing Systems* **32**. Curran Associates, Inc., pp 8024–8035, <http://papers.neurips.cc/paper/9015-pytorch-an-imperative-style-high-performance-deep-learning-library.pdf>
- Pillepich A., et al., 2018, *MNRAS*, **475**, 648
- Press W. H., Schechter P., 1974, *ApJ*, **187**, 425
- Ronneberger O., Fischer P., Brox T., 2015, in Navab N., Hornegger J., Wells W. M., Frangi A. F., eds, *Medical Image Computing and Computer-Assisted Intervention – MICCAI 2015*. Springer International Publishing, Cham, pp 234–241
- Rouhiainen A., Giri U., Münchmeyer M., 2021, arXiv e-prints, p. [arXiv:2105.12024](https://arxiv.org/abs/2105.12024)
- Scaramella R., et al., 2021, arXiv e-prints, p. [arXiv:2108.01201](https://arxiv.org/abs/2108.01201)
- Schaye J., et al., 2015, *MNRAS*, **446**, 521
- Sheth R. K., Tormen G., 1999, *MNRAS*, **308**, 119
- Springel V., White M., Hernquist L., 2001, *ApJ*, **549**, 681
- Springel V., et al., 2005, *Nature*, **435**, 629
- The EAGLE team 2017, arXiv e-prints, p. [arXiv:1706.09899](https://arxiv.org/abs/1706.09899)
- Tinker J., Kravtsov A. V., Klypin A., Abazajian K., Warren M., Yepes G., Gottlöber S., Holz D. E., 2008, *ApJ*, **688**, 709
- Van Rossum G., Drake F. L., 2009, *Python 3 Reference Manual*. CreateSpace, Scotts Valley, CA

Villaescusa-Navarro F., et al., 2021a, arXiv e-prints, [p. arXiv:2109.09747](https://arxiv.org/abs/2109.09747)
 Villaescusa-Navarro F., et al., 2021b, arXiv e-prints, [p. arXiv:2109.10360](https://arxiv.org/abs/2109.10360)
 Virtanen P., et al., 2020, *Nature Methods*, **17**, 261
 Vogelsberger M., et al., 2014a, *MNRAS*, **444**, 1518
 Vogelsberger M., Zavala J., Simpson C., Jenkins A., 2014b, *Monthly Notices of the Royal Astronomical Society*, **444**, 3684
 Vogelsberger M., Marinacci F., Torrey P., Puchwein E., 2020, *Nature Reviews Physics*, **2**, 42
 Wadekar D., Villaescusa-Navarro F., Ho S., Perreault-Levasseur L., 2020, arXiv e-prints, [p. arXiv:2012.00111](https://arxiv.org/abs/2012.00111)
 Warren M. S., Abazajian K., Holz D. E., Teodoro L., 2006, *ApJ*, **646**, 881
 Xu X., Ho S., Trac H., Schneider J., Poczos B., Ntampaka M., 2013, *The Astrophysical Journal*, **772**, 147
 Xu X., Kumar S., Zehavi I., Contreras S., 2021, *MNRAS*, **507**, 4879
 York D. G., et al., 2000, *AJ*, **120**, 1579
 Zavala J., Frenk C. S., 2019, *Galaxies*, **7**, 81
 Zhao X., Mao Y., Cheng C., Wandelt B. D., 2022, *ApJ*, **926**, 151
 da Costa-Luis C., et al., 2021, tqdm: A fast, Extensible Progress Bar for Python and CLI, [doi:10.5281/zenodo.4663456](https://doi.org/10.5281/zenodo.4663456), <https://doi.org/10.5281/zenodo.4663456>

APPENDIX A: SAMPLING THE HALO MASS FUNCTION

The sampling can be described in two steps. First, we convert the halo mass function into a probability density function (PDF). We want to sample haloes with masses in the range $(10^9, 10^{12}) M_\odot$, since this is also the mass range which corresponds to the haloes in the images of Fig. 2. Therefore, the PDF of the halo mass function can be calculated as

$$\text{PDF}(M) = \frac{b \left(\frac{M}{M_\odot}\right)^{-a}}{\int_{10^9}^{10^{12}} b \left(\frac{M}{M_\odot}\right)^{-a} d\left(\frac{M}{M_\odot}\right)} = \frac{(1-a)}{(10^{12})^{1-a} - (10^9)^{1-a}} \cdot \left(\frac{M}{M_\odot}\right)^{-a}. \quad (\text{A1})$$

Then, we sample from this PDF by using inverse transform sampling (Devroye 1986). The cumulative distribution function of the PDF of the halo mass function, can be calculated as

$$F(M) = \frac{\int_{10^9}^M \left(\frac{M'}{M_\odot}\right)^{-a} d\left(\frac{M'}{M_\odot}\right)}{\int_{10^9}^{10^{12}} \left(\frac{M'}{M_\odot}\right)^{-a} d\left(\frac{M'}{M_\odot}\right)} = \quad (\text{A2})$$

$$= \frac{\left(\frac{M}{M_\odot}\right)^{1-a} - (10^9)^{1-a}}{(10^{12})^{1-a} - (10^9)^{1-a}}, \quad (\text{A3})$$

for $M \in (10^9, 10^{12}) M_\odot$. Solving the equation

$$y = \frac{\left(\frac{M}{M_\odot}\right)^{1-a} - (10^9)^{1-a}}{(10^{12})^{1-a} - (10^9)^{1-a}} \quad (\text{A4})$$

for $\frac{M}{M_\odot}$ in terms of y , yields

$$F^{-1}(y) = (y \cdot (10^{12})^{1-a} - y \cdot (10^9)^{1-a} + (10^9)^{1-a})^{\frac{1}{1-a}}. \quad (\text{A5})$$

Therefore, the samples are the values of function $F^{-1}(y)$ for $y \in (0, 1)$.

As we can see from eq. (A1), the sampling procedure does not depend on the normalization, b , of the halo mass function. Thus, b is not a parameter of our model. On the contrary, the inner slope of the halo mass function, a , is the second parameter of our model. Nevertheless, the value of b can be calculated from eq. (1) along with the number, N , of haloes as

$$\begin{aligned} \frac{dn}{dM} &= b \left(\frac{M}{M_\odot}\right)^{-a} \Rightarrow \\ \int_{N_1}^{N_2} dn &= \int_{10^9}^{10^{12}} b \left(\frac{M}{M_\odot}\right)^{-a} dM \Rightarrow \\ \int_{N_1}^{N_2} dn &= \int_{10^9}^{10^{12}} b \left(\frac{M}{M_\odot}\right)^{-a} d\left(\frac{MM_\odot}{M_\odot}\right) \Rightarrow \\ \frac{N_2 - N_1}{V} &= \frac{N}{V} = b \left(\frac{(10^{12})^{1-a}}{1-a} - \frac{(10^9)^{1-a}}{1-a}\right) M_\odot \Rightarrow \\ b &= (1-a) \cdot \frac{N}{((10^{12})^{1-a} - (10^9)^{1-a})VM_\odot} \quad (\text{A6}) \end{aligned}$$

Thus

$$b = (1-a) \cdot \frac{N}{((10^{12})^{1-a} - (10^9)^{1-a})V} [\text{Mpc}^{-3} M_\odot^{-1}]. \quad (\text{A7})$$

APPENDIX B: EFFECTIVE CLUSTERING MODEL

B1 Realizations of Gaussian Fields on an $M \times M$ grid

To generate realizations of a Gaussian perturbation field, δ , which has a power spectrum given by a power-law, i.e., $P(k) = k^{-n}$, we will first generate a field $\varphi_{\mathbf{k}}$ which has a unit amplitude, i.e., $\langle \varphi_{\mathbf{k}} \varphi_{-\mathbf{k}} \rangle = 1$. Then, we can create the field, δ , which has the desired power spectrum, $P(k)$, by defining $\delta_{\mathbf{k}} \equiv P^{1/2}(k) \varphi_{\mathbf{k}}$ since

$$\langle \delta_{\mathbf{k}} \delta_{-\mathbf{k}} \rangle = P(k) \langle \varphi_{\mathbf{k}} \varphi_{-\mathbf{k}} \rangle = P(k). \quad (\text{B1})$$

A field which has a constant power spectrum is a white noise field for which:

$$\begin{aligned} \langle \varphi(\mathbf{x}) \varphi(\mathbf{y}) \rangle &= A \delta^d(\mathbf{x} - \mathbf{y}) \text{ and} \\ P(k) &= A, \quad (\text{B2}) \end{aligned}$$

i.e., for which there are no correlations between the fluctuations at different points. Therefore, to generate a field, $\varphi_{\mathbf{k}}$, that has a unit amplitude, we pick $A=1$ and we get

$$\langle \varphi(\mathbf{x}) \varphi(\mathbf{y}) \rangle = \delta^d(\mathbf{x} - \mathbf{y}). \quad (\text{B3})$$

To create a realisation of white noise on an $M \times M$ grid -where M is an even number- we first replace the field $\varphi(\mathbf{x})$ with discrete values $\varphi_{ab}^{\mathbf{x}}$, where $a, b \in \{0, 1, \dots, M-1\}$, which are drawn from the probability distribution function

$$\mathcal{P}[\varphi_{ab}^{\mathbf{x}}] = \prod_{c,d=0}^{M-1} \frac{\exp\left[-\frac{1}{2}(\varphi_{cd}^{\mathbf{x}})^2\right]}{\sqrt{2\pi}}. \quad (\text{B4})$$

Therefore, to generate a white noise realisation we choose randomly, for every grid point, a value from a standard normal distribution.

Now, we will work in Fourier space, since we want to generate a field that has a desired power spectrum. First, we Fourier transform the white noise realization. On the grid, the continuous Fourier transform that relates $\phi(\mathbf{x})$ and $\varphi_{\mathbf{k}}$ is replaced by the discrete Fourier transform

$$\begin{aligned} \varphi_{ab}^{\mathbf{k}} &= \sum_{c,d=0}^{M-1} \exp(-ix_c k_a - ix_d k_b) \varphi_{cd}^{\mathbf{x}} \\ \varphi_{ab}^{\mathbf{x}} &= \frac{1}{M^2} \sum_{c,d=0}^{M-1} \exp(ix_c k_a + ix_d k_b) \varphi_{cd}^{\mathbf{k}}, \quad (\text{B5}) \end{aligned}$$

where $x_a = a$ and $k_a = \frac{2\pi a}{M}$. We also know that φ_{ab}^x is real so we have

$$\varphi_{ab}^{*x} = \varphi_{ab}^x \Rightarrow \varphi_{ab}^{*k} = \varphi_{-a-b}^k. \quad (\text{B6})$$

Moreover, eq. (B5) can also be evaluated outside of the domain $a, b \in \{0, 1, \dots, M-1\}$ and the extended sequence is M -periodic. Thus, we have

$$\varphi_{ab}^x = \varphi_{(a+nM)b}^x = \varphi_{a(b+nM)}^x \text{ where } n \in \mathbb{Z} \quad (\text{B7})$$

and we also get

$$\varphi_{a(\frac{M}{2}+b)}^{*k} = \varphi_{-a-(\frac{M}{2}+b)}^k = \varphi_{M-a-(\frac{M}{2}-b+M)}^k = \varphi_{(M-a)(\frac{M}{2}-b)}^k \quad (\text{B8})$$

and

$$\varphi_{(\frac{M}{2}+a)b}^{*k} = \varphi_{-(\frac{M}{2}+a)-b}^k = \varphi_{(-\frac{M}{2}-a+M)(M-b)}^k = \varphi_{(\frac{M}{2}-a)(M-b)}^k. \quad (\text{B9})$$

Now, as we saw before, we have to multiply the Fourier space realisation of the white noise with the square root of the desired power spectrum, and the resulting field has to obey eq. (B6) and eq. (B7), as well as eq. (B8) and eq. (B9). If we would just multiply the Fourier space grid realization of the white noise with the square root of the power spectrum evaluated at points k , where $k = \frac{2\pi}{M} \sqrt{a^2 + b^2}$ with $a, b \in \{0, 1, \dots, M-1\}$, then we would find

$$\delta_{a(\frac{M}{2}+b)}^{*k} \neq \delta_{(M-a)(\frac{M}{2}-b)}^k \quad (\text{B10})$$

and

$$\delta_{(\frac{M}{2}+a)b}^{*k} \neq \delta_{(\frac{M}{2}-a)(M-b)}^k, \quad (\text{B11})$$

because of the power spectrum factor. If we would then transform the resulting field back to the position space, we would have an imaginary field δ_{ab}^{*x} . One way to overcome this problem is to define the field δ_{ab}^k as

$$\delta_{ab}^k = \begin{cases} P^{1/2}(k) \varphi_{ab}^k & k = \frac{2\pi}{M} \sqrt{a^2 + b^2} \text{ and } a, b \leq M/2 \\ P^{1/2}(k) \varphi_{a(b-M)}^k & k = \frac{2\pi}{M} \sqrt{a^2 + (b-M)^2} \text{ and } a \leq M/2, b > M/2 \\ P^{1/2}(k) \varphi_{(a-M)b}^k & k = \frac{2\pi}{M} \sqrt{(a-M)^2 + b^2} \text{ and } a > M/2, b \leq M/2 \\ P^{1/2}(k) \varphi_{(a-M)(b-M)}^k & k = \frac{2\pi}{M} \sqrt{(a-M)^2 + (b-M)^2} \text{ and } a, b > M/2. \end{cases} \quad (\text{B12})$$

Because of eq. (B7) we can also write

$$\delta_{ab}^k = \begin{cases} P^{1/2}(k) \varphi_{ab}^k & k = \frac{2\pi}{M} \sqrt{a^2 + b^2} \text{ and } a, b \leq M/2 \\ P^{1/2}(k) \varphi_{ab}^k & k = \frac{2\pi}{M} \sqrt{a^2 + (b-M)^2} \text{ and } a \leq M/2, b > M/2 \\ P^{1/2}(k) \varphi_{ab}^k & k = \frac{2\pi}{M} \sqrt{(a-M)^2 + b^2} \text{ and } a > M/2, b \leq M/2 \\ P^{1/2}(k) \varphi_{ab}^k & k = \frac{2\pi}{M} \sqrt{(a-M)^2 + (b-M)^2} \text{ and } a, b > M/2 \end{cases} \quad (\text{B13})$$

or, alternatively, we can define

$$\delta_{(a+M)(b+M)}^k = \delta_{ab}^k = P^{1/2}(k) \varphi_{ab}^k = P^{1/2}(k) \varphi_{(a+M)(b+M)}^k, \quad (\text{B14})$$

where $k = \frac{2\pi}{M} \sqrt{a'^2 + b'^2}$, with $a', b' \in \{0, \dots, M/2, -M/2+1, \dots, -1\}$. The real, position space field then reads

$$\delta_{ab}^x = \frac{1}{M^2} \sum_{c,d=0}^{M-1} \exp(ix_c k_a + ix_d k_b) \delta_{cd}^k. \quad (\text{B15})$$

Equivalently, to generate 2D realizations of Gaussian fields, one could use available Python packages, e.g., *powerbox* (Murray 2018).

B2 Application to mock data generation

To generate realizations of the Gaussian fields and thus to add clustering to our model, we follow the procedure described in Appendix B1. First, we start by generating a position space realization of a white noise field φ_{ab}^x with unit amplitude, on a $M \times M$ grid, i.e., $a, b \in \{0, \dots, M-1\}$. Since images in Fig. 2 are generated by 2D histograms with 100 bins, we pick $M=100$. We call this grid, the “sampling grid”, in order to avoid confusion with other grids that will be defined. Afterwards, we Fourier transform the white noise realization ($\varphi_{ab}^x \rightarrow \varphi_{ab}^k$) and we multiply it with the square root of the power spectrum, $P(k)$ of eq. (2). Finally, we perform an inverse Fourier transform to return back to position space and get the desired realization, δ_{ab}^{*x} . Fig. D1 illustrates 2D realizations of Gaussian fields generated from power spectra with different slopes.

B3 Sampling positions of haloes

To obtain the positions of the haloes, we randomly sample from the field f and the samples that we obtain are i and j indices of the 100×100 “sampling grid” (see Appendix B2). Moreover, we define a new 100×100 grid, called the “coordinate grid”, whose values correspond to pairs of x and y coordinates where $(x, y) \in (0, 12.5)$ Mpc. Then, the positions X and Y of the haloes are given by the values x and y of the “coordinate” grid, at the indices that we previously sampled from the “sampling grid”.

Once we obtain the positions of the haloes, we place each one of them in the 2D-sky. This process is accomplished in four steps. We start by subtracting the coordinates of each of the N haloes (as pairs of X, Y values) from the values of the “coordinate grid”. In this way, we construct N 100×100 grids. Then, for each of these grids, we calculate the root sum square of the two values in each one of its cells. If we think of the grids as images and their cells as pixels, this means that the value of each pixel corresponds to the distance between the center of the pixel and a fixed reference, which is the position of the halo. To further clarify that, in each grid we calculate the projected radius, r' , of each halo.

APPENDIX C: SIMULATION BASED INFERENCE

C1 Loss function

Following Hermans et al. (2020), the loss functional

$$L[d_\phi(\mathbf{x}, \theta)] = \int d\theta \int d\mathbf{x} p(\mathbf{x}, \theta) [-\log d_\phi(\mathbf{x}, \theta)] + p(\theta) p(\mathbf{x}) [-\log(1 - d_\phi(\mathbf{x}, \theta))] \quad (\text{C1})$$

is minimized for a function $d^*(\mathbf{x}, \theta)$ such that

$$\begin{aligned} \frac{\delta}{\delta \phi} L[d_\phi(\mathbf{x}, \theta)]|_{d^*} &= 0 \Rightarrow \\ -\frac{\delta}{\delta \phi} \int d\theta \int d\mathbf{x} p(\mathbf{x}, \theta) [\log d_\phi(\mathbf{x}, \theta)] + p(\theta) p(\mathbf{x}) [\log(1 - d_\phi(\mathbf{x}, \theta))] &= 0. \end{aligned} \quad (\text{C2})$$

This equation holds for any $\frac{\delta d_\phi(\mathbf{x}, \theta)}{\delta \phi}$, so according to the fundamental lemma of calculus of variations we have

$$-\frac{p(\mathbf{x}, \theta)}{d_\phi^*(\mathbf{x}, \theta)} + \frac{p(\theta) p(\mathbf{x})}{1 - d_\phi^*(\mathbf{x}, \theta)} = 0. \quad (\text{C3})$$

As long as $p(\theta) > 0$, eq. (C3) leads to the decision function

$$\begin{aligned} \frac{p(\mathbf{x}, \theta)}{d_\phi^*(\mathbf{x}, \theta)} &= \frac{p(\mathbf{x})p(\theta)}{1 - d_\phi^*(\mathbf{x}, \theta)} \Leftrightarrow \\ d_\phi^*(\mathbf{x}, \theta) &= \frac{p(\mathbf{x}, \theta)}{p(\mathbf{x}, \theta) + p(\mathbf{x})p(\theta)}. \end{aligned} \quad (\text{C4})$$

C2 Neural Ratio Estimation (NRE)

Following Hermans et al. (2020), eq. (15) can be rewritten as

$$d(\mathbf{x}, \theta) \approx \frac{p(\theta|\mathbf{x})p(\mathbf{x})}{p(\theta|\mathbf{x})p(\mathbf{x}) + p(\mathbf{x})p(\theta)} = \frac{\frac{p(\theta|\mathbf{x})}{p(\theta)}}{\frac{p(\theta|\mathbf{x})}{p(\theta)} + 1}. \quad (\text{C5})$$

The ratio

$$r(\mathbf{x}, \theta) \equiv \frac{p(\mathbf{x}|\theta)}{p(\mathbf{x})} = \frac{p(\theta|\mathbf{x})}{p(\theta)} \quad (\text{C6})$$

can be then approximated from eq. (C5) as

$$\begin{aligned} d(\mathbf{x}, \theta) &\approx \frac{\frac{p(\theta|\mathbf{x})}{p(\theta)}}{\frac{p(\theta|\mathbf{x})}{p(\theta)} + 1} = \frac{r(\mathbf{x}, \theta)}{r(\mathbf{x}, \theta) + 1} \Leftrightarrow \\ r(\mathbf{x}, \theta)d(\mathbf{x}, \theta) - r(\mathbf{x}, \theta) &\approx d(\mathbf{x}, \theta) \Leftrightarrow \\ r(\mathbf{x}, \theta) &\approx \frac{d(\mathbf{x}, \theta)}{d(\mathbf{x}, \theta) - 1} \Leftrightarrow \\ \frac{p(\theta|\mathbf{x})}{p(\theta)} &\approx \frac{d(\mathbf{x}, \theta)}{d(\mathbf{x}, \theta) - 1}. \end{aligned} \quad (\text{C7})$$

The approximation of the ratio allows us finally to estimate directly the posterior $p(\theta|\mathbf{x})$ as

$$p(\theta|\mathbf{x}) \approx \frac{d(\mathbf{x}, \theta)}{d(\mathbf{x}, \theta) - 1} p(\theta) = \hat{p}(\theta|\mathbf{x}). \quad (\text{C8})$$

C3 Marginal Neural Ration Estimation (MNRE)

As exactly described in Section 2.3.1, *swyft* trains binary classifiers $d_{k,\phi}(\mathbf{x}, \boldsymbol{\theta}_k)$ in parallel, where, now, each one depends on the parameters of interest $\boldsymbol{\theta}_k$, to distinguish jointly drawn from marginally drawn parameter-simulation pairs. The ratios of interest $r_k(\mathbf{x}, \boldsymbol{\theta}_k)$ can be then estimated as

$$r_k(\mathbf{x}, \boldsymbol{\theta}_k) \approx \frac{d_{k,\phi}(\mathbf{x}, \boldsymbol{\theta}_k)}{1 - d_{k,\phi}(\mathbf{x}, \boldsymbol{\theta}_k)} = \hat{r}_k(\mathbf{x}, \boldsymbol{\theta}_k) \quad (\text{C9})$$

and the corresponding posteriors $p(\boldsymbol{\theta}_k|\mathbf{x})$ can be estimated as

$$p(\boldsymbol{\theta}_k|\mathbf{x}) \approx r_k(\mathbf{x}, \boldsymbol{\theta}_k)p(\boldsymbol{\theta}_k) = \hat{p}(\boldsymbol{\theta}_k|\mathbf{x}). \quad (\text{C10})$$

Practically, estimating the ratio using eq. (C9) is susceptible to numerical errors since the ratio is computed by transforming the sigmoid function (Hermans et al. 2020). Thus, *swyft* uses an modified network architecture which directly outputs the value of the NN $f_{k,\phi}$ (Miller et al. 2021), instead of $\sigma \circ f_{k,\phi}$ which the majority of the binary classifiers output. Since $\sigma(x)$ is defined by the formula

$$\sigma(x) = \frac{e^x}{1 + e^x}, \quad (\text{C11})$$

eq. (C5), which describes the output of a typical classifier, after being adjusted to marginals, can be written as

$$d_{k,\phi}(\mathbf{x}, \boldsymbol{\theta}_k) \approx \frac{\frac{p(\boldsymbol{\theta}_k|\mathbf{x})}{p(\boldsymbol{\theta}_k)}}{\frac{p(\boldsymbol{\theta}_k|\mathbf{x})}{p(\boldsymbol{\theta}_k)} + 1} = \sigma \circ \log\left(\frac{p(\boldsymbol{\theta}_k|\mathbf{x})}{p(\boldsymbol{\theta}_k)}\right) = \quad (\text{C12})$$

$$= \sigma \circ \log(r_k(\mathbf{x}, \boldsymbol{\theta}_k)). \quad (\text{C13})$$

Therefore, the modified classifier implies

$$f_{k,\phi} = \log(r_k(\mathbf{x}, \boldsymbol{\theta}_k)). \quad (\text{C14})$$

Using eq. (17) we can then estimate the marginal posteriors as

$$p(\boldsymbol{\theta}_k|\mathbf{x}) \approx e^{f_{k,\phi}} p(\boldsymbol{\theta}_k) = \hat{p}(\boldsymbol{\theta}_k|\mathbf{x}). \quad (\text{C15})$$

APPENDIX D: 2D REALIZATIONS OF GAUSSIAN FIELDS

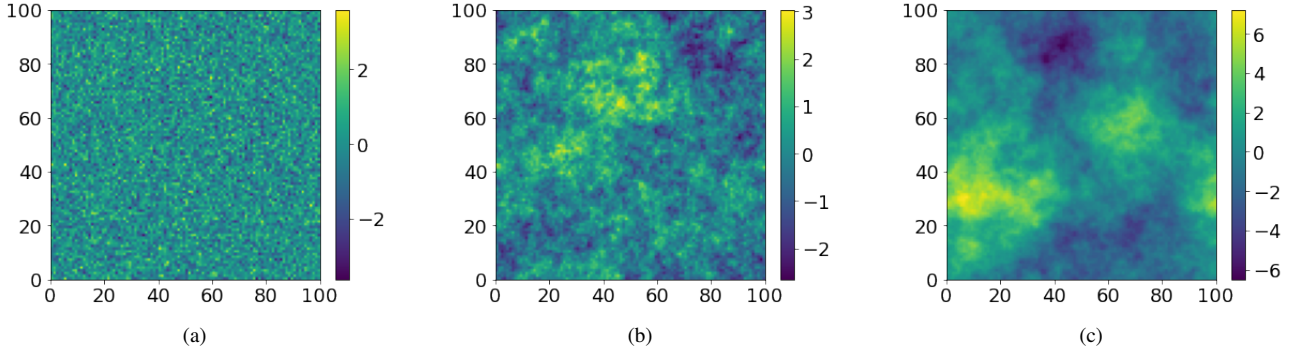


Figure D1. Realizations of power spectra of the form $P(k) = k^{-n}$ on three 100×100 grids. Each grid corresponds to a different slope n with $n \in \{0, 2, 4\}$. The $n = 0$ realization (Fig. D1a) is white noise, while the length scale over which fluctuations are correlated increases as n increases.

APPENDIX E: COMPARISON OF N-BODY SIMULATION AND MOCK IMAGES

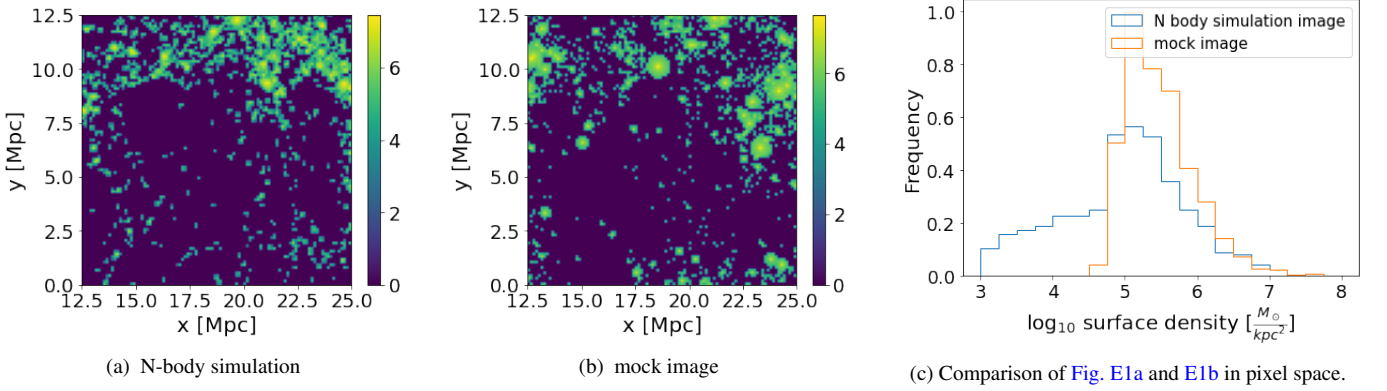


Figure E1. Comparison of an N-body simulation and an mock image which have the same number of haloes, N , and the same inner slope, a of the halo mass function. The mock image was chosen in order for the clustering of the haloes to visually correspond to that of the N-body simulation image. From the histograms of Fig. E1c, we see that the distributions of the surface densities in pixel space are similar to each other. However, small differences between them are spotted, especially towards low surface densities produced by the boundaries of the haloes. This is unsurprising, since our model is not perfect and, as described in Section 2.2, we defined an artificial boundary for the haloes in the mock images.

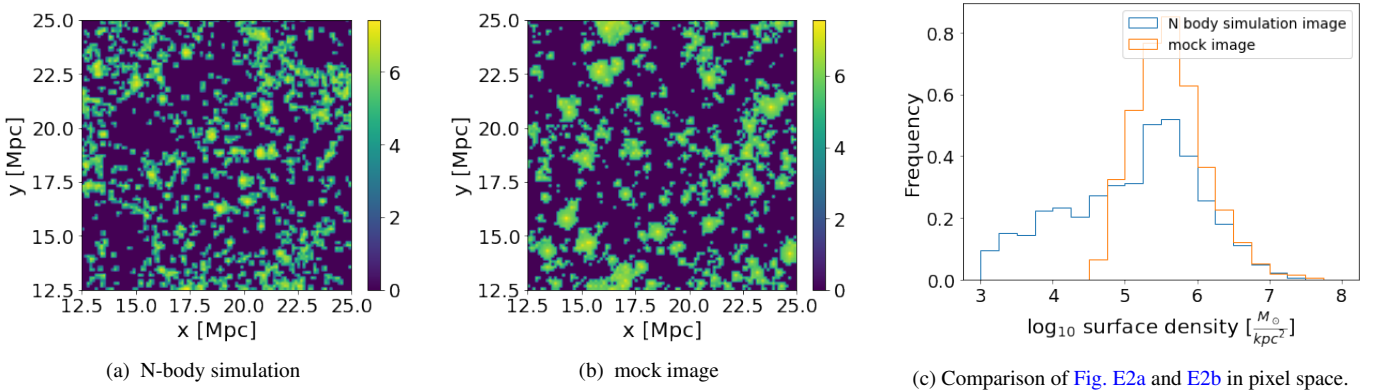


Figure E2. Like Fig. E1, but the images are generated using a larger \log_{10} cutoff, c , of the halo mass function.

This paper has been typeset from a $\text{\TeX}/\text{\LaTeX}$ file prepared by the author.